New Journal of Physics
The open access journal at the forefront of physics

Deutsche Physikalische Gesellschaft DPG
IOP Institute of Physics

Published in partnership with: Deutsche Physikalische Gesellschaft and the Institute of Physics

OPEN ACCESS

RECEIVED
31 October 2015

REVISED
9 February 2016

ACCEPTED FOR PUBLICATION
22 February 2016

PUBLISHED
7 March 2016

PAPER

Quantitative two-dimensional strain mapping of small core–shell FePt@Fe_3O_4 nanoparticles

Marianne Monteforte[1,2], Shoko Kobayashi[3], Le D Tung[4], Koichi Higashimine[3], Derrick M Mott[5], Shinya Maenosono[5], Nguyen T K Thanh[2,4] and Ian K Robinson[1,4,6,7]

[1] London Centre for Nanotechnology, University College London, WC1E 6BT, UK
[2] UCL Healthcare Biomagnetics and Nanomaterials Laboratory, 21 Albemarle Street, London, W1S 4BS, UK
[3] Center for Nano Materials and Technology, Japan Advanced Institute of Science and Technology (JAIST), 1-1 Asahidai, Nomi, Ishikawa 923-1292, Japan
[4] Department of Physics & Astronomy, University College, London, WC1E 6BT, UK
[5] School of Materials Science, Japan Advanced Institute of Science and Technology (JAIST), 1-1 Asahidai, Nomi, Ishikawa 923-1292, Japan
[6] Research Complex at Harwell, Rutherford Appleton Laboratory, Didcot, Oxon, OX11 0FA, UK
[7] Author to whom any correspondence should be addressed.

E-mail: i.robinson@ucl.ac.uk

Keywords: core–shell, nanoparticle structure, lattice strain, geometric phase

Supplementary material for this article is available online

Abstract

We report a facile one-pot chemical synthesis of colloidal FePt@Fe_3O_4 core–shell nanoparticles (NPs) with an average diameter of 8.7 $\pm$ 0.4 nm and determine their compositional morphology, microstructure, two-dimensional strain, and magnetic hysteresis. Using various state-of-the-art analytical transmission electron microscopy (TEM) characterization techniques—including high resolution TEM imaging, TEM tomography, scanning TEM-high angle annular dark field imaging, and scanning TEM-energy dispersive x-ray spectroscopy elemental mapping—we gain a comprehensive understanding of the chemical and physical properties of FePt@Fe_3O_4 NPs. Additional analysis using x-ray photoelectron spectroscopy, x-ray diffraction, and superconducting quantum interference device magnetometry distinguishes the oxide phase and determines the magnetic properties. The geometric phase analysis method is effective in revealing interfacial strain at the core–shell interface. This is of fundamental interest for strain engineering of nanoparticles for desirable applications.

Abbreviations

NPs	Nanoparticles
fcc	Face-centred cubic
XRD	X-ray diffraction
XPS	X-ray photoelectron spectroscopy
ICP-OES	Inductively coupled plasma optical emission spectroscopy
TEM	Transmission electron microscopy
STEM	Scanning TEM

HRTEM	High resolution TEM
GPA	Geometric phase analysis
FC	Field cooled
ZFC	Zero field cooled

1. Introduction

FePt nanoparticles (NPs) represent a diverse class of alloy with a specific attraction over pure metal counterparts due to their high magneto-crystalline anisotropy and chemical stability. Coating FePt NPs with a biocompatible layer such as iron oxide is of practical interest because it can lower the cytotoxicity, and allows for direct bio-functionalization of the nanoparticle surface (Kalambur *et al* 2005, Lai *et al* 2008, Krishnan 2010, Thanh and Green 2010). Thus FePt@Fe_3O_4 NPs are of specific interest for biomedical applications such as hyperthermia and targeted drug delivery (Sahu *et al* 2015). Additionally, FePt@Fe_3O_4 NPs are of interest for potential applications in electromagnetic devices (Carpenter *et al* 2003), nano-catalytic devices (Wu *et al* 2012, Wang *et al* 2015) and permanent magnetic data storage media (Saita and Maenosono 2005). Previous magnetic studies of spherical FePt@Fe_3O_4 NPs identified exchange coupling effects between the magnetically 'hard' FePt core and the magnetically 'soft' Fe_3O_4 shell (Zeng *et al* 2004) causing a smooth co-operative magnetic switching transition at the core–shell interface. The chemical synthetic procedures and magnetic properties of these FePt@Fe_3O_4 NPs have been a primary source of scientific interest (Yang *et al* 2015) and yet there have been very few investigations into the exchange–coupling interface, which can be directly impacted by the compositional 3D morphology, elemental distribution, and interfacial strain. Understanding the strain present in core–shell NPs is beneficial in applications to mass transport devices (Pratt *et al* 2014) and catalytic reduction reactions (Gan *et al* 2012). Therefore, developing an effective method to quantitatively map the strain gradients in these FePt@Fe_3O_4 NPs is of fundamental importance.

Electron tomography has been well developed for determining the 3D morphology of macroscopic systems, such as biological specimens, but is still a considerably new technique in its application to nanomaterials and, in particular, NPs. Scott *et al* (2012) have already demonstrated the extent of the data attainable using 3D electron tomography to analyse a 10 nm Au NP, identifying individual dislocations at a resolution of 2.4 Å. Also, Florea *et al* (2012) made a complete structural analysis of 5 nm diameter Pt NPs, confirming the usefulness of the tomography approach. In the study reported here, a 3D reconstruction of a FePt@Fe_3O_4 NP is built from a series of 61 electron micrographs, collected over a tilt series of $\pm 60^\circ$ (in 2° increments) from transmission electron microscopy (TEM) images. The 'missing-wedge' of information, due to restrictions in the tilt range of the specimen goniometer, is overcome by applying a relatively new topography based reconstruction (TBR) algorithm. TBR uses a density constraint within a defined volume, leading to a cleaner reconstruction in comparison with the conventional weighted Fourier back projection reconstruction methods of Weyland *et al* (2001).

Strain analysis using coherent x-ray diffraction (XRD) is a well-developed technique for the quantitative analysis of the 3D structure and strain fields present in NPs (Newton *et al* 2010). It is however limited to a current spatial resolution limit of ~20 nm. Alternative synchrotron-based strain analysis methods have been adopted for analysis of NPs below this size limit. Extended x-ray absorption fine structure reveals the atomic bond distances of the surface atoms (Strasser *et al* 2010). High energy powder XRD provides an insight into high resolution lattice information manifested in the diffraction pattern of NPs (Kuo *et al* 2013). More conventional strain analysis methods have been applied to nanostructured materials, such as scanning electron microscopy (SEM) cross sectioning (Usuda *et al* 2005) which is intrusive for nanoparticles as the lamellar cross sectioning in SEM can induce/remove any internal strain. Less-intrusive methods, such as aberration corrected scanning TEM (STEM), have been adopted to quantify lattice deviations associated with the strain release mechanisms in core–shell NPs by Bhattarai *et al* (2013). This gives an indication of the extent of the strain but has not yet provided a clear picture of strain gradients throughout the nanoparticle structure. A powerful extension to this direct STEM method is the geometric phase analysis (GPA) technique, developed by Hytch *et al* (1989, 2003), which enables the quantitative mapping of 2D strain fields from a crystal system. A recent study by Pratt *et al* (2014) investigated the strain fields within the shell of Fe@Fe_3O_4 NPs using GPA analysis. These authors found that strain gradients arose from confined oxide domain formation within the shell, which enhanced ionic movement. The GPA approach opens an opportunity to investigate the strain fields within a whole nanoparticle and correlate them with their compositional morphology and magnetic properties.

In the work presented here, spherical 8.71 ± 0.44 nm FePt@Fe_3O_4 NPs were synthesised using a facile chemical thermal decomposition method by the chemical reduction of $Pt(acac)_2$ (5×10^{-4} mmol) and thermal decomposition of $Fe(CO)_5$ (4×10^{-3} mmol) in the presence of stabilising surfactants oleylamine

(4×10^{-3} mmol) and oleic acid (4×10^{-3} mmol). In our synthesis, adapted from the procedure of Nandwana *et al* (2007), $Pt(acac)_2$ was added into the reaction flask—using an inert moisture-free reflux environment—containing 20 ml of degassed solvent octa-1-decene. The reaction vessel was purged (at room temperature) under a blanket of nitrogen for 30 min whilst magnetic stirring at 500 rpm. Subsequently the temperature of the reaction vessel was raised to 107 °C at a rate of 4 °C per min. The reaction vessel temperature was maintained at 107 °C for two min during the addition of 1.88 ml olelyamine and 1.28 ml oleic acid followed by the injection of 100 μl of pure $Fe(CO)_5$ precursor (resulting in the reaction solution changing hue from yellow to black suggesting the formation of NPs in the solution). The temperature of the reaction vessel was then raised to 120 °C and an additional 100 μl of $Fe(CO)_5$ was injected into the reaction mixture. This controlled addition of excess $Fe(CO)_5$ precursor is intended to grow the shell after all the $Pt(acac)_2$ has been consumed. The reaction vessel temperature was then raised at rate of 8 °C per min to 250 °C and maintained at this temperature to reflux for 30 min. The heat source was then removed and the reaction vessel cooled to room temperature. The reaction mixture was collected and dispersed in ethanol (with a 1:1 ratio) and cleaned by centrifugation. The NP product was then dispersed in 5 ml hexane, and precipitated out by adding 10 ml of ethanol followed by centrifugation (repeated twice). The final clean NP product was re-dispersed in hexane for storage and analysis.

The FePt@Fe_3O_4 NPs were quantified by the following methods: (i) conventional TEM for size distribution analysis, (ii) inductively coupled plasma optical emission spectroscopy (ICP-OES) for chemical composition determination, (iii) conventional powder XRD for phase determination and (iv) x-ray photoelectron spectroscopy (XPS) for chemical surface compositional analysis to distinguish the complex composition of the Fe oxide shell. The XPS data measurements were acquired using a Shimadzu Kratos AXIS-ULTRA delay-line detector high-performance XPS system, operating at a vacuum level of 10^{-7} Torr. Photoelectrons were excited by monochromatic aluminium K_α radiation (emitted from an x-ray tube operating at 150 W) and focused on the centre of the specimen surface irradiating an area of 300×700 μm^2. State-of-the-art TEM techniques were then applied to probe the atomic scale properties of the FePt@Fe_3O_4 NPs. These included (i) STEM-high angle annular dark field (STEM-HAADF) for high contrast lattice imaging, (ii) STEM-energy dispersive x-ray spectroscopy (STEM-EDS) for elemental mapping and (iii) electron tomography for visualisation of the 3D morphology and segmentation of the core and shell, that cannot be obtained from 2D TEM imaging methods alone.

2. Sample quantification

2.1. Crystallographic study

From the TEM observations, the FePt@Fe_3O_4 NPs formed 2D self-assembled hexagonal arrays on the substrate, as seen in figures 1(a) and (b). It can be seen that there is a homogenous coating of Fe oxide and a clear minimum particle separation distance of 1.7 nm, which corresponds to a compacted surfactant layer with the surfactant tails interpenetrating. The fully-extended lengths of the oleic acid and oleylamine surfactants are 2.08 nm and 2.06 nm, respectively.

The average size of the FePt@Fe_3O_4 NPs is 8.7 ± 0.4 nm (calculated from 309 particles), and the average sizes of the FePt core and the Fe_3O_4 shell are 7.0 ± 0.5 nm and 1.5 ± 0.2 nm, respectively. High resolution TEM (HRTEM) imaging of single FePt@Fe_3O_4 NPs, as shown in figure 1(c), enabled the contrast between the core and shell to be identified, due to the different electron penetration efficiencies. The single crystal core has an interplanar spacing of 1.94 Å (yellow in figure 1(c)) which is characteristic of the (100) lattice planes in the chemically disordered face-centred cubic (fcc) FePt phase.

XRD analysis of the FePt@Fe_3O_4 core–shell NPs in figure 2 revealed the characteristic peaks of chemically-disordered fcc FePt material. The observed XRD lines match closely to the reference pattern platinum ferroan, $Fe_{0.8}Pt_{3.2}$ (JPCDS. 029-0717). Additional XRD peaks are ascribed to the contribution from the Fe_3O_4 shell, as indicated by the reference pattern magnetite, (JCPDS-075-1372). The lack of prominent peaks from the Fe oxide is expected to be due to the lower volume fraction of Fe oxide in comparison to FePt as also observed by Sahu *et al* (2015). The lattice parameters of $Fe_{0.8}Pt_{3.2}$ and Fe_3O_4 were identified as 3.887 Å and 8.396 Å, respectively. The composition of the $Fe_{0.8}Pt_{3.2}$ reference match corresponds reasonably to the ICP-OES results; where atomic percent of Fe is 31% and atomic percent of Pt is 69%.

2.2. Surface composition study

The deconvolved XPS spectra of Fe 2p, Pt 4f, and O 1s core level spectra are shown in figures 3(a), (b) and (c) respectively. The Fe 2p spectrum in figure 3(a) is composed of two peaks at Fe $2p_{3/2}$ and Fe $2p_{1/2}$ at a binding energy (BE) of 713.5 eV and 731.6 eV, respectively.

The Fe 2p spectrum in figure 3(a) was deconvolved into five different Fe species, including Fe^0, Fe^{2+}, Fe^{3+} high-binding energy surface structures (Grosvenor 2004, Aronniemi *et al* 2005) and satellite peaks using a

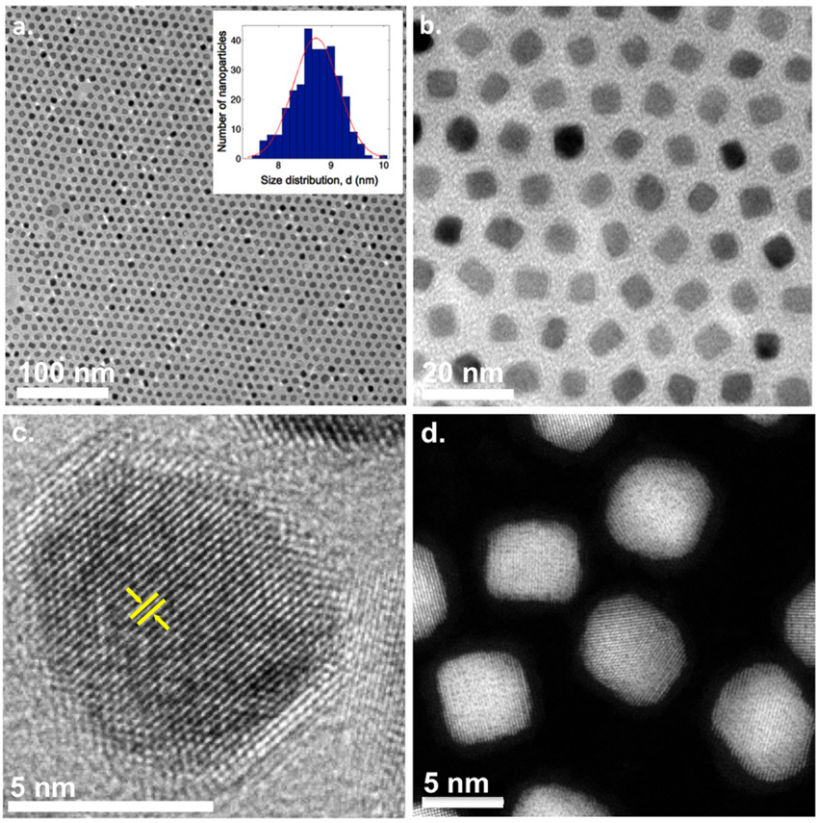

Figure 1. FePt@Fe_3O_4 NPs TEM analysis (a) low magnification and (b) high magnification TEM image of FePt@Fe_3O_4 NPs showing a 2D hexagonal array with a size distribution histogram inset (average diameter 8.7 $\pm$ 0.4 nm) (c) HRTEM image of an individual FePt@Fe_3O_4 nanoparticle with the inter-planar lattice spacing of the FePt core denoted in yellow (d) STEM-HAADF image (corresponding STEM-EDS in figures 6 (a)–(d)).

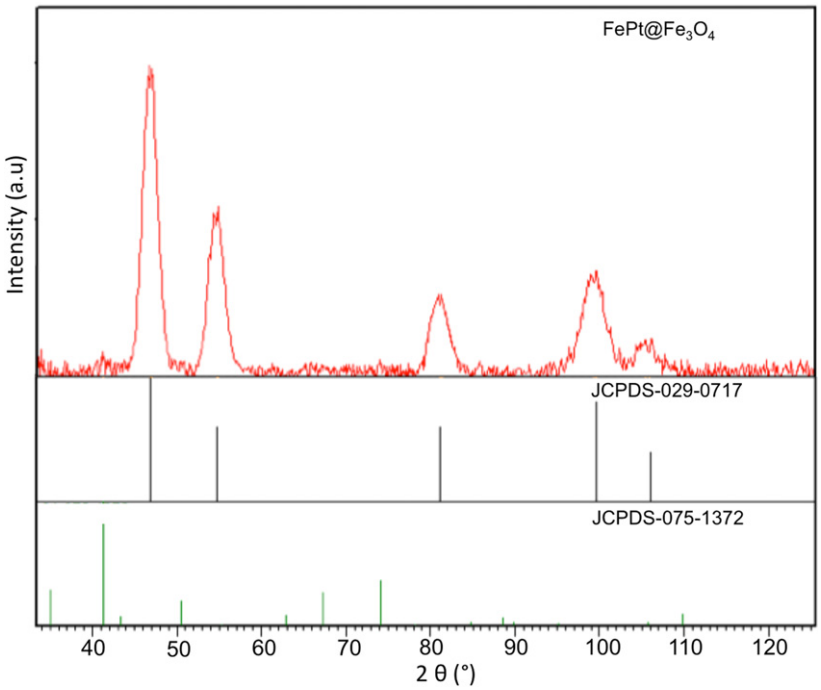

Figure 2. Powder XRD of FePt@Fe_3O_4 core–shell NPs with corresponding reference pattern of the prominent $Fe_{0.8}Pt_{3.2}$ fcc phase (JCPDS-029-0717) and the Fe_3O_4 phase indicated by its reference pattern (JCPDS-075-1372).

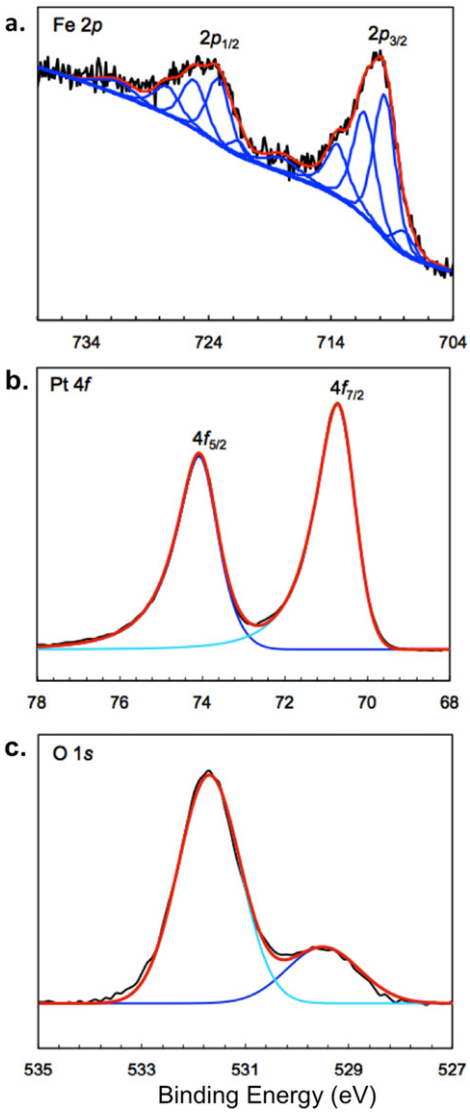

Figure 3. Deconvolved x-ray photoelectron spectroscopy spectra (a) Fe 2p spectrum, (b) Pt 4f spectrum, with spin–orbit splitting into $4f_{7/2}$ and $4f_{5/2}$, (c) O 1s spectrum. Light and dark blue curves are the individual peaks, whose sum gives the red curve fitting the data (black).

Gaussian−Lorentzian mixed function by XPSPEAK41 software. The $2p_{3/2}$ peak was deconvolved into three peaks; Fe^0 at a BE of 708.0 eV, Fe^{2+} at a BE of 709.6 eV, and Fe^{3+} at a BE of 711.3 eV with a satellite peak at 718.0 eV. The $2p_{1/2}$ peak is deconvolved into Fe^0 at a BE of 721.6 eV, Fe^{2+} at BE 723.2 eV, and Fe^{3+} at a BE of 725.2 eV with a satellite peak at 731.6 eV. The stoichiometric proportion values of Fe^0, Fe^{2+}, Fe^{3+} were calculated, based on the XPS analysis, as $Fe^0 = 7\%$, $Fe^{2+} = 52\%$, and $Fe^{3+} = 41\%$. Theoretically, the stoichiometric bulk proportion of Fe^{2+} in Fe_2O_3 is 0%, Fe_3O_4 is 33% and FeO is 100%, while the proportion of Fe^{3+} in Fe_2O_3 is 100%, Fe_3O_4 is 67% and FeO is 0%. While we have insufficient information to assign the oxide fractions categorically, the simultaneous presence of both extremes is considered less likely than the mixed oxide because they would interconvert. If all the Fe^{3+} were in Fe_3O_4 this would account for 41% of Fe^{3+} and 20.5% of Fe^{2+} leaving a balance of 31.5% of the Fe in the form of FeO (wustite).

The Pt 4f spectrum in figure 3(b) is composed of two peaks indicating spin–orbit split doublet of Pt into $4f_{5/2}$ and $4f_{7/2}$ at a BE of 70.72 eV and 74.08 eV respectively, with a separation in energy of 3.5 eV, which is typical for metallic FePt. The O 1s signal in figure 3(c) is composed of two peaks at lower and intermediate BE's at 529.5 eV and 531.7 eV, as a result of the iron oxide shell. The XPS results substantiate the TEM and XRD data, and confirm the formation of the Fe oxide phase as Fe_3O_4.

2.3. Morphological study

The distribution and morphology of a cluster of nine FePt@Fe_3O_4 NPs was analysed by TEM tomography. The resulting 3D Hitachi reconstructions are shown in figures 4(a)–(c) at different ortho-slice positions, slicing

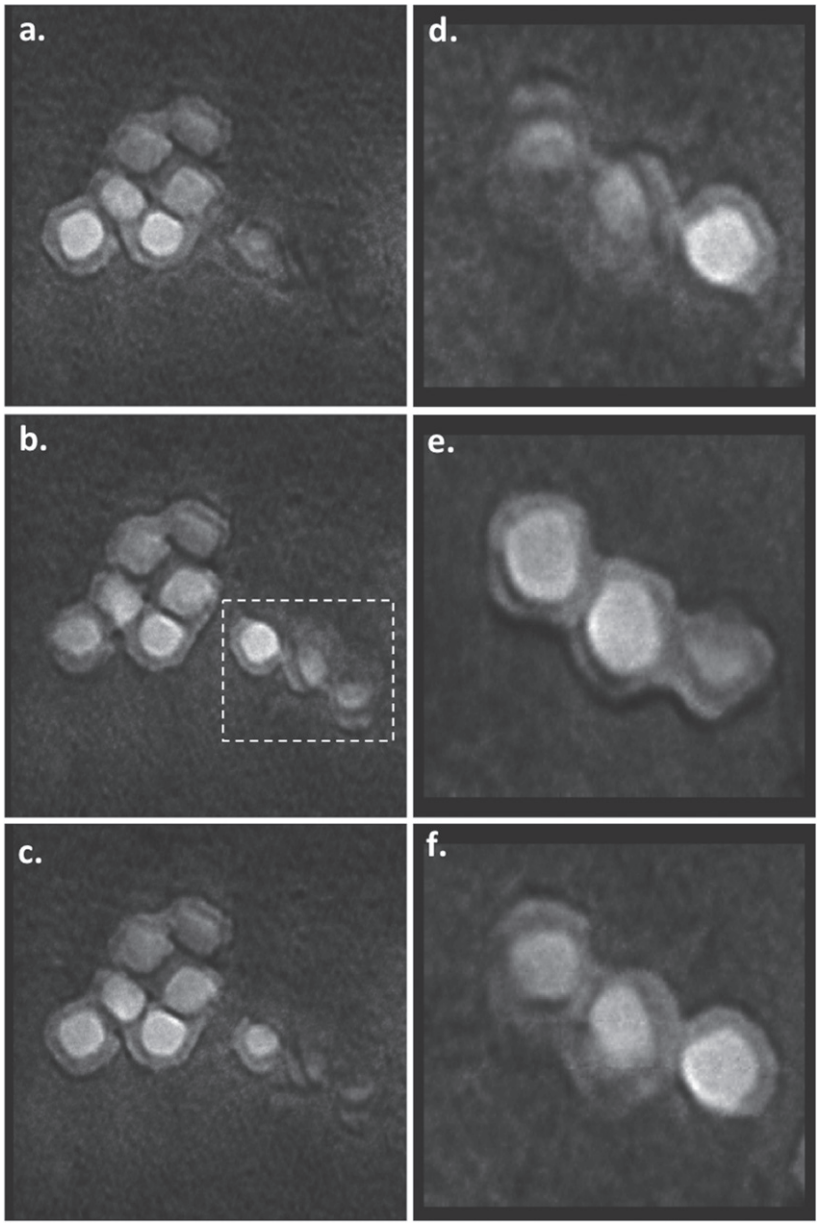

Figure 4. 3D Hitachi reconstruction of a cluster of nine FePt@Fe_3O_4 NPs at y ortho-slice positions: (a) $y = 5$, (b) $y = +10$, (c) $y = +20$, and corresponding zoom of three particles from the region indicated by the dashed box at (d) $y = -10$, (e) $y = -5$, and (f) $y = 0$.

through the y-axis of the reconstruction. The lower three NPs (indicated by the box in figure 4(c) were examined more closely in figures 4(d)–(f), demonstrating the core–shell morphology; where the Fe_3O_4 shell is distinguished from the FePt core by its lower contrast due to the shell being less electron-dense. An Avizo reconstruction (and supplementary movie) was built in order to visualise and segment the cluster into the nine NPs from the raw TEM reconstructed data. The core can be differentially segmented from the shell as illustrated in figure 5(a), where the FePt core is shown in yellow and the Fe_3O_4 shell in grey. An ortho-slice through the centre of the cluster is shown in figure 5(b) where the FePt core is represented in light blue and the Fe_3O_4 shell in dark blue for clarity. The core can be differentially segmented from the shell as illustrated in figure 5(a), where the external FePt core is represented in yellow and the external Fe_3O_4 shell in grey.

2.4. Compositional study

Elemental distribution maps were acquired for the FePt@Fe_3O_4 NPs using STEM-EDS elemental mapping. The corresponding STEM-HAADF image is shown in figure 1(d). The O K-edge elemental contribution (represented in green) in figure 6(a) is homogenously distributed throughout both the core and the shell of the nanoparticle and is clearly higher than the typical background due to contamination. The Fe K-edge elemental contribution (represented in red) in figure 6(b) is also homogeneously distributed throughout the core and shell,

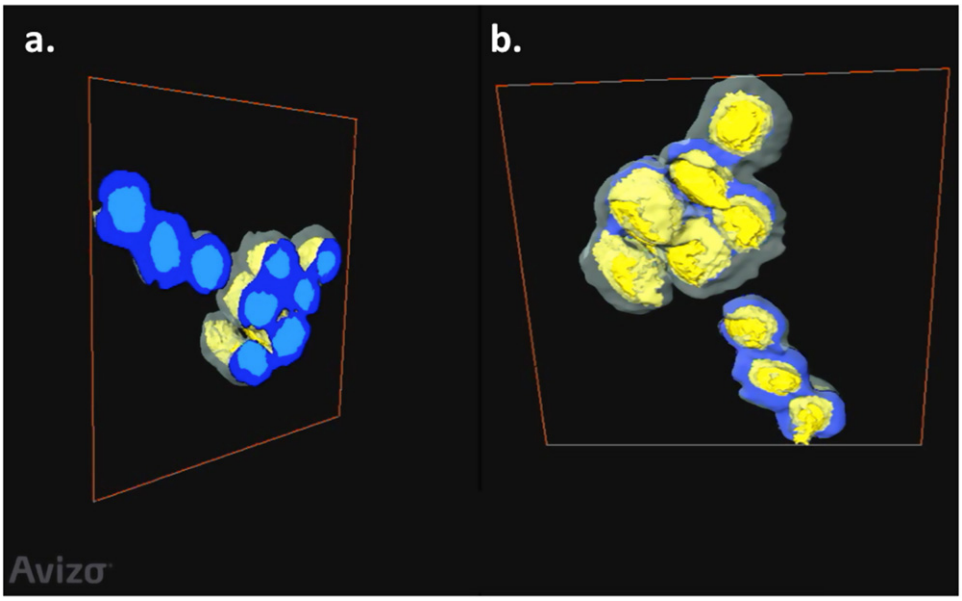

Figure 5. Avizo reconstruction of a cluster of nine FePt@Fe_3O_4 NPs enclosed in a bounding box (a) ortho-slice through the centre of the cluster that distinguishes the internal FePt core (light blue) and the internal Fe_3O_4 shell (dark blue) (b) corresponding snap shot of the external 3D reconstruction showing the external FePt core (yellow) and external Fe_3O_4 shell (grey). For a movie sweeping through the cross sections, see the supplementary movie.

with a more prominent contribution from the shell. The Pt M-edge elemental contribution (represented in blue) in figure 6(c) is distributed only in the core. An overlay of the three elemental maps is shown in figure 6(d) and confirms the presence of the Fe oxide shell. The line profiles across of the O K-edge, Fe K-edge and, Pt M-edge are shown in figure 6(e). The rectangular integration regions are shown in figures 6(a)–(c). The intensity profiles quantitatively demonstrate that the higher Pt signal is localised in the core while the Fe and O contributions extend beyond the core into the shell.

3. Strain analysis

3.1. Geometric phase analysis

Strain can, in principle, be seen in lattice images of materials, such as those of figure 1. However, the Fourier dark-field filtering capability of the GPA method allows the slow-varying distortions of the lattice to be extracted for quantitative evaluation. The GPA method used here was implemented with a MatLab script used to evaluate the HRTEM images in three steps: (i) the nanoparticle image is isolated by manual masking from its neighbours (ii) the masked image density is Fourier transformed with an FFT (iii) a Bragg peak from the crystal lattice is isolated and cut out from the bright field diffraction pattern (iv) this local region of the diffraction pattern is recentred and inverse Fourier transformed back to a real space complex image (v) the amplitude of the real space complex image closely resembles the original crystal and (vi) the phase of the real space complex image is a projection of the lattice distortions in the direction of the selected Bragg peak. This method has a close similarity to the Bragg coherent diffraction imaging method of imaging strains with x-rays (Robinson and Harder 2009).

In the case of a core–shell structure made of two dissimilar materials, an important question is whether the core–shell interface is strained or relaxed. Aranda *et al* (2010) showed that a crystal of a material with one lattice constant appears as a linear phase ramp in the phase image calculated in the coordinate system of the other crystal. The direction of the phase ramp is given by the direction of the Bragg peak used for imaging. The same result is expected for GPA of a FePt@Fe_3O_4 nanoparticle: in the coordinate system of the FePt, the Fe_3O_4 will be expected to show a linear variation of phase in the direction of the Bragg peak selected for the dark-field imaging. Any deviation from this behaviour can be interpreted as strain relaxation. Conversely, any dislocations that may form at the interface will show up as localised phase structures, so long as their Burgers vector is not the same as the imaging Bragg peak.

Strain analysis by GPA, was applied to the masked STEM-HAADF image of the isolated FePt@Fe_3O_4 nanoparticle (in figure 7(c)), resulting reciprocal space diffraction pattern of figure 7(a).
A single Bragg spot was selected, as circled in figure 7(a) (with a radius cut off of 35 pixels), and re-centred in figure 7(b). The selected peak is a (200) peak of the FePt lattice, so it is the distortions from the {100} planes that

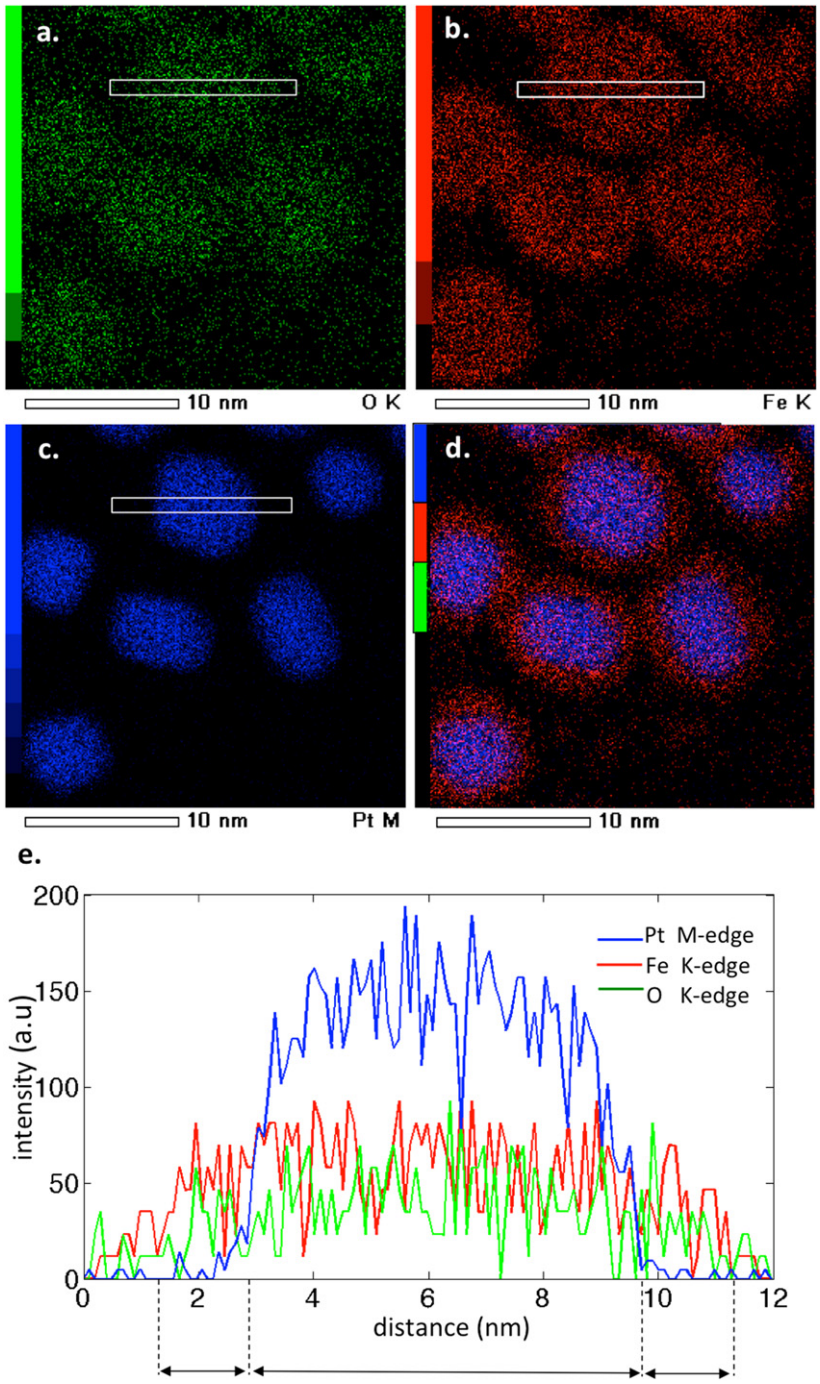

Figure 6. STEM-EDS elemental mapping images of FePt@Fe_3O_4 NPs (a) O K-edge (b) Fe K-edge (c) Pt M-edge (d) elemental overlay and, (e) corresponding intensity profiles of rectangular ROI's through the centre of an individual FePt@Fe_3O_4 nanoparticle (corresponding to the STEM-HAADF image in figure 1(d).

are imaged by GPA. The region of reciprocal space surrounding this selected Bragg spot, sufficiently large to include the interference from the overlapping Bragg peaks of the Fe oxide shell, was Fourier transformed into a real space complex image; the geometric phase is shown in figure 7(e) and the image amplitude in figure 7(f). The STEM-EDS elemental map of the same crystal is reproduced in figure 7(d) showing the approximate location of the core–shell interface. The geometric phase image in figure 7(e), a map of the 2D strain projection, represents the displacement of atoms from the perfect crystal lattice, ranging from $-\pi$ (black) to $+\pi$ (white), shows the strain along the (200) direction. The full phase range of 2π corresponds to a displacement of a single lattice spacing. Note that the phase becomes meaningless in the regions outside the nanoparticle, where the amplitude of the complex density drops to zero.

The core and shell can be clearly distinguished in figure 7(e) by the phase shift enclosing the shell (dark region). There are slight deviations from the median value within the core which might be due to defects,

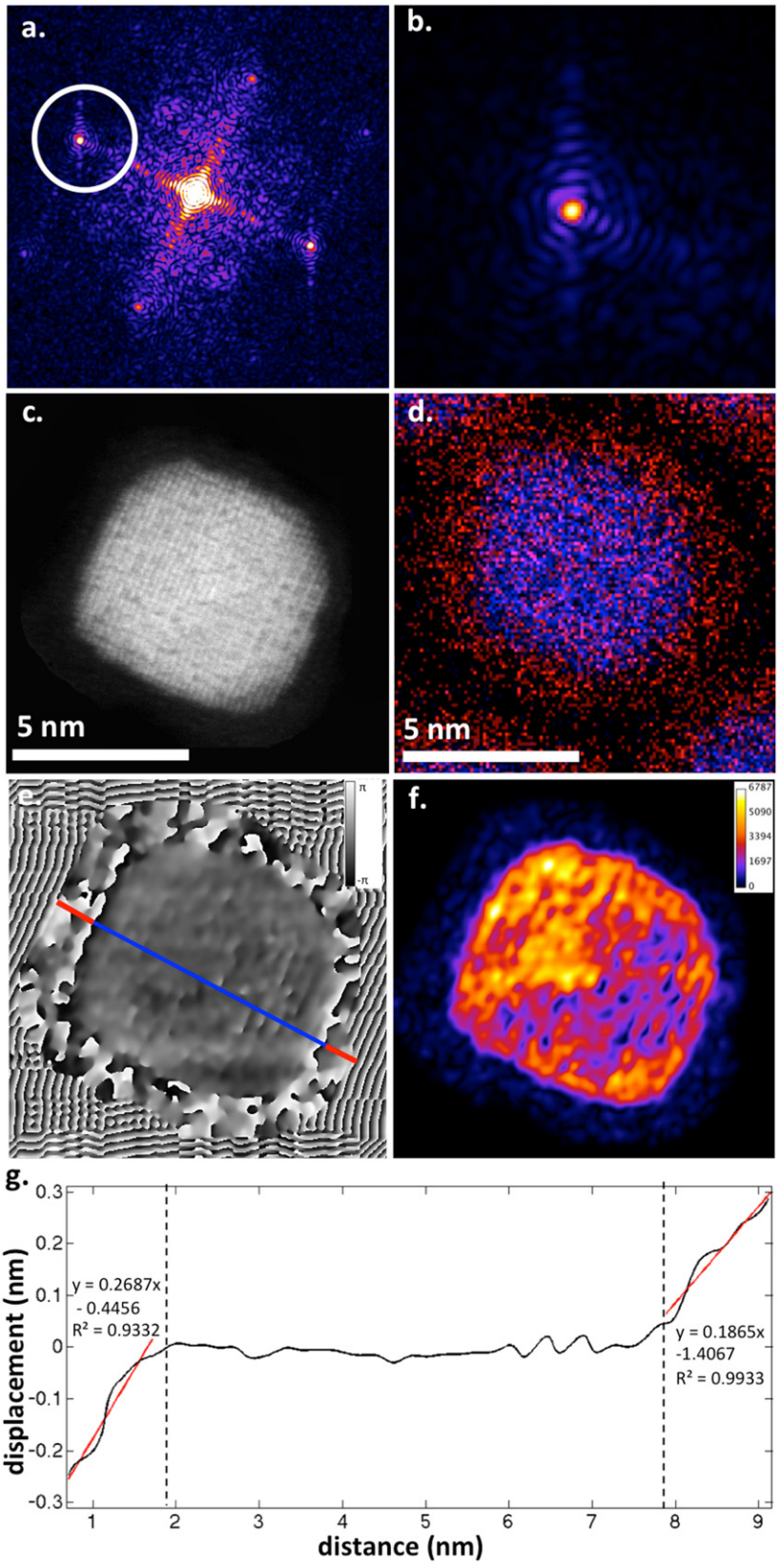

Figure 7. 2D strain analysis of an isolated FePt@Fe_3O_4 nanoparticle (a) calculated reciprocal space pattern of the masked STEM-HAADF image (b) re-centred Fourier filtered Bragg spot (c) masked STEM-HAADF image with a high threshold (blue) to distinguish shell (d) STEM-EDS map of an overlay of the Fe K-edge (red), O K-edge (green) and Pt K-edge (blue) elemental distributions (e) real space geometric phase map of the local displacement of the lattice fringes with a cross section line indicating the core (blue) and the shell (red). Phase values run from $-\pi$ (black) to π (white). (f) Real space local amplitude image (with intensity scale inset) (g) cross section plot of the phase variation with phase slope change at the core indicated by the dashed lines.

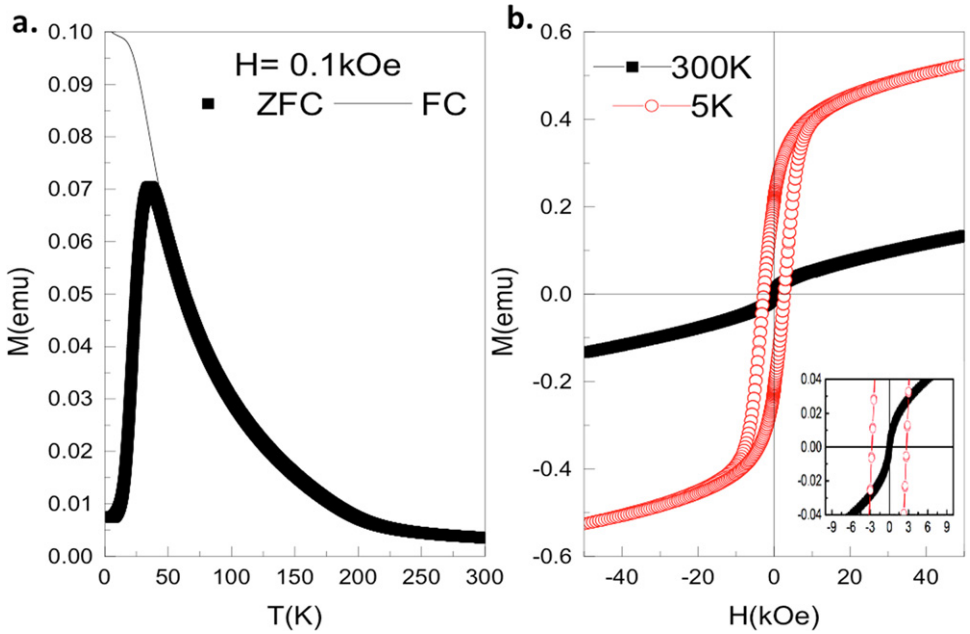

Figure 8. (a) Zero-field-cooled (ZFC) and field-cooled (FC) magnetisation curves in a measuring field of 100 Oe; (b) hysteresis loops measured at 300 K and 5 K.

possibly dislocations, in the FePt crystal structure. Regions of high strain gradients and phase wraps surrounding the core of the nanoparticle are due to the strains present in the Fe_3O_4 shell, which is seen to be less homogeneous than the core. Some of these apparent strain inhomogeneities could also be due to local compositional variations of the oxide. The local amplitude image in figure 7(f) shows this intensity variation in the selected (200) plane direction, with an intensity scale ranging from pink (high intensity) to green (low intensity).

In order to examine the strain decay behaviour at the core–shell interface the cross section line in figure 7(e), covering the core (blue) and the shell (red) regions, is plotted in figure 7(g). The linear phase ramps seen on the two sides of figure 7(g) represent the difference in lattice constant between the FePt, and the Fe_3O_4. The location of the core–shell interface is indicated by the dashed lines with the shell thickness being 1.39 nm on the left and 1.54 nm on the right, corresponding to an average shell thickness of 1.5 nm. A clear phase ramp can be seen on both sides of the particle, whose direction across the scan from negative to positive indicates an inward compressive strain (Aranda *et al* 2010). Strains (displacement gradients) of 27% and 19% ($\pm$4%) were extracted from the least squares regression fits of the positive and negative phase ramps, indicated in figure 7(e). Based on the known 1.94 Å lattice spacing of the FePt core, this gives spacings for the Fe_3O_4 shell of 2.46 Å and 2.31 Å.

3.2. Magnetic properties

Figure 8(a) shows a plot of the zero-field-cooled (ZFC) and field-cooled (FC) magnetisation versus temperature curves measured in a field of 100 Oe. In the ZFC curve, we observed a peak at a blocking temperature T_B of about 35 K associated with the transition from the superparamagnetic state to blocked state of the magnetic NPs with decreasing temperature. Below the blocking temperature, $T_B = 35$ K, the ZFC and FC curves significantly diverge and the NPs are in the ferromagnetic blocked state.

Well above T_B, the ZFC and FC curves coincide due to the fact that all NPs are at the same superparamagnetic state. The sharp peak in the ZFC curve at T_B is an evidence of a narrow energy barrier distribution, or equivalently, a narrow T_B distribution, which is in accordance with the narrow monodispersity of the size distribution of our synthesised NPs. The isothermal hysteresis loops of the as-prepared FePt@Fe_3O_4 NPs carried out at temperature of 300 K and 5 K are presented in figure 8(b). At low temperature, well below T_B, the loop is open with the coercivity H_c of about 2.7 kOe. There are no steps seen in the hysteresis loop at 5 K which would have been an indication of two uncoupled separate magnetic phases with different remanent magnetisations and coercivities. Similar to what has been reported by Zheng *et al* (2004), the observed smooth change of the magnetisation with magnetic field in the hysteresis loop measured at 5 K suggests that the FePt core and Fe_3O_4 shell in our sample are in intimate contact and fully exchange–coupled.

4. Conclusion

In conclusion, an adapted synthetic method was used to fabricate core–shell FePt@Fe_3O_4 NPs by thermal decomposition creating the shell by controlled addition of excess $Fe(CO)_5$ precursor. The resultant magnetic nanoparticle suspension was of narrow size distribution and highly monodisperse forming 2D self-assembled hexagonal arrays on the substrate, which is desirable for magnetic data storage applications. The high-resolution lattice spacing information acquired from HRTEM images of the NPs enabled phase identification of both the core (chemically disordered fcc FePt phase) and the shell (Fe_3O_4 phase) and the XRD showed a corresponding mixed phase pattern. Additionally, XPS surface analysis of the NPs distinguished the phase of the oxide as Fe_3O_4 (magnetite) rather than Fe_2O_3 (maghaemite). The STEM elemental distribution maps showed the localised distribution of Pt within the core region only and a more homogenous distribution of Fe, with a slightly higher contribution in the shell. The 3D reconstructions and visualisations from the TEM tomography data show a distinct segmentation of the FePt core from the Fe_3O_4 shell.

Strain maps of the strain displacement fields in individual FePt@Fe_3O_4 NPs were acquired using GPA mapping of the STEM lattice images. This showed a clear interface between the core and the shell, with a highly strained shell. The strain seen in the oxide shell appeared to be the result of the interfacial lattice mismatch which was quantified to be 23%. The lattice strain induced in the shell by the core is attractive for many potential applications for example in, mass transport devices in catalytic and nanoscale multiferroic applications. Mapping the presence/absence of this strain is therefore useful in the development of these functional NP materials. The magnetic data, showing a smooth change of the magnetisation with applied magnetic field, correlates with the 2D strain mapping observations and suggests that the FePt core and Fe_3O_4 shell are in intimate contact and thus exchange–coupled. The complementary characterisation methods used within this study enabled a comprehensive analysis of the elemental, morphological, magnetic and, strain effects of core–shell NPs, which is of fundamental interest in the fine-tuning of these NP materials for applications.

Author contributions

The manuscript was written through contributions of all authors. All authors have given approval to the final version of the manuscript.

Funding sources

This work was sponsored by a studentship to Marianne Monteforte from the Diamond Light Source, an EPSRC grant EP/I022562/1 'Phase modulation technology for x-ray imaging', an ERC Advanced Grant 227711 'Exploration of strains in synthetic nano crystals', and the Japan Society for the Promotion of Science (JSPS) Summer Program. N T K Thanh thanks the Royal Society for her University Research Fellowship. L D Tung thanks AFOSR for funding.

References

Aranda M A G, Berenguer F, Bean R J, Shi X, Xiong G, Collins S P, Nave C and Robinson I K 2010 Coherent x-ray diffraction characterization of twinned microcrystals *J. Synchrotron Radiat.* **17** 751–60

Aronniemi R, Sainio and Lahtinen J 2005 *J. Surf. Sci.* **578** 108–23

Bhattarai N, Casillas G, Ponce A and Jose-Yacaman M 2013 Strain-release mechanisms in bimetallic core–shell nanoparticles as revealed by Cs-corrected STEM *Surf. Sci.* **609** 161–4

Carpenter E E, Calvin S, Stroud R M and Harris V G 2003 *Chem. Mater.* **15** 3245–6

Florea I, Demortière A, Petit C, Bulou H, Hirlimann C and Ersen O 2012 *ACS Nano* **6** 2574–81

Gan L, Yu R, Luo J, Cheng Z and Zhu J 2012 Lattice strain distributions in individual dealloyed PtFe catalyst nanoparticles *J. Phys. Chem. Lett.* **3** 934–8

Grosvenor A P, Kobe B A, Biesinger M C and McIntyre N S 2004 *Surf. Interface Anal.* **36** 1564–74

Hytch M J, Snoeck E and Kilaas R 1998 *Ultramicroscopy* **74** 131–46

Hytch M J, Putaux J L and Penisson J M 2003 Measurement of the displacement field of dislocations to 0.03 angstrom by electron microscopy *Nature* **423** 270–3

Kalambur V S, Han B, Hammer B E, Shield T W and Bischof J C 2005 *Nanotechnology* **16** 1221–33

Krishnan K M 2010 *IEEE Trans. Magn.* **46** 2523–58

Kuo C-H, Lamontagne L, Brodsky C, Chou L-Y, Zhuang J, Sneed B, Sheehan M and Tsung C-K 2013 The effect of lattice strain on the catalytic properties of Pd nanocrystals *Chem. Sus. Chem.* **6** 1993–2000

Lai C-W, Wang Y-H, Uttam B P, Chen Y-C, Hsiao J-K, Liu C-L, Liu H-M, Chen C-Y and Chou P-T 2008 One-pot solvothermal synthesis of FePt/Fe_3O_4 core–shell nanoparticles *Chem. Commun.* **42** 5342–4

Nandwana V, Elkins K E, Poudyal N, Chaubey G S, Yano K and Liu J P 2007 Size and shape control of monodisperse FePt nanoparticles *J. Phys. Chem.* C **111** 4185–9

Newton M C, Leake S J, Harder R and Robinson I K 2010 Three-dimensional imaging of strain in a single ZnO nanorod *Nat. Mater.* **9** 120–4

Pratt A, Lari L, Hovorka O, Shah A, Woffinden C, Tear S P, Binns C and Krager R 2014 *Nat. Mater.* **13** 26–30
Robinson I K and Harder R 2009 Coherent diffraction imaging of strains on the nanoscale *Nat. Mater.* **8** 291–8
Saita S and Maenosono S 2005 FePt nanoparticles with a narrow composition distribution synthesized via pyrolysis of iron(III) ethoxide and platinum(II) acetylacetonate *Chem. Mater.* **17** 3705–10
Sahu N K, Gupta J and Bahadur D 2015 PEGylated FePt–Fe_3O_4 composite nanoassemblies (CNAs): *in vitro* hyperthermia, drug delivery and generation of reactive oxygen species (ROS) *Dalton Trans.* **44** 9103
Scott M C, Chen C C, Mecklenburg M, Zhu C, Xu R, Ercius P, Dahmen U, Regan B C and Miao J 2012 *Nature* **483** 444–7
Strasser P *et al* 2010 *Nat. Chem.* **2** 454–60
Thanh N T K and Green L A W 2010 *Nano Today* **5** 213–30
Usuda K, Numata T, Irisawa T, Hirashita N and Takagi S 2005 Strain characterization in SOI and strained-Si on SGOI MOSFET channel using nano-beam electron diffraction (NBD) *Mater. Sci. Eng.* B **124** 143–7
Wang D-Y, Chou H-L, Cheng C-C, Wu Y-H, Tsai C-M, Lin H-Y, Wang Y-L, Hwang B-J and Chen C-C 2015 FePt nanodendrites with high-index facets as active electrocatalysts for oxygen reduction reaction *Nano Energy* **11** 631–9
Weyland M, Midgley P A and Thomas J M 2001 *J. Phys. Chem.* B **105** 7882–6
Wu J, Zhu J, Zhou M, Hou Y and Gao S 2012 FePt concave nanocubes with enhanced methanol oxidation activity *Cryst. Eng. Comm.* **14** 7572–5
Yang W, Lei W, Yongsheng Y, Zhu W, George T A, Li X-Z, Sellmyer D J and Sun S 2015 From FePt–Fe_3O_4 to L_{10}-FePt–Fe nanocomposite magnets with a gradient interface *J. Mater. Chem.* C **3** 7075
Zeng H, Sun S, Li J, Wang Z L and Liu J P 2004 *Appl. Phys. Lett.* **85** 792–4